Stabilizing Nanocrystalline Oxide Nanofibers at Elevated Temperatures by Coating Nanoscale Surface Amorphous Films

Lei Yao,[†] Wei Pan,*[,†] Jian Luo,*[,‡] Xiaohui Zhao,[†] Jing Cheng,[†] and Hiroki Nishijima[§]

[†]State Key Lab. of New Ceramics and Fine Processing, School of Materials Science and Engineering, Tsinghua University, Beijing, 100084, People's Republic of China

[‡]Department of NanoEngineering, Program of Materials Science and Engineering, University of California, San Diego, La Jolla, California 92093-0448, United States

[§]Functional Material Department, Inorganic Material Engineering Division, Toyota Motor Corporation, Toyota, Aichi 471-8572, Japan

S *Supporting Information*

ABSTRACT: Nanocrystalline materials often exhibit extraordinary mechanical and physical properties but their applications at elevated temperatures are impaired by the rapid grain growth. Moreover, the grain growth in nanocrystalline oxide nanofibers at high temperatures can occur at hundreds of degrees lower than that would occur in corresponding bulk nanocrystalline materials, which would eventually break the fibers. Herein, by characterizing a model system of scandia-stabilized zirconia using hot-stage in situ

scanning transmission electron microscopy, we discover that the enhanced grain growth in nanofibers is initiated at the surface. Subsequently, we demonstrate that coating the fibers with nanometer-thick amorphous alumina layer can enhance their temperature stability by nearly 400 °C via suppressing the surface-initiated grain growth. Such a strategy can be effectively applied to other oxide nanofibers, such as samarium-doped ceria, yttrium-stabilized zirconia, and lanthanum molybdate. The nanocoatings also increase the flexibility of the oxide nanofibers and stabilize the high-temperature phases that have 10 times higher ionic conductivity. This study provides new insights into the surface-initiated grain growth in nanocrystalline oxide nanofibers and develops a facile yet innovative strategy to improve the high-temperature stability of nanofibers for a broad range of applications.

KEYWORDS: *Nanocrystalline oxide nanofibers, nanocoating, grain growth, thermal stability, surface energy*
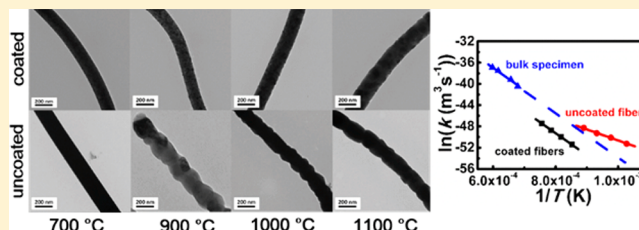
When the size of a grain, or a crystallite in a polycrystal, is reduced below 100 nm, grain boundary effects begin to dominate its property.[1−3] As such, various interesting and useful properties emerge in the nanocrystalline materials.[4−10] Polycrystalline oxide nanofibers, wherein both the grain size and diameter are on nanoscale, have great potential for various applications due to their unique electrical, optical, magnetic, and thermal properties as well as extraordinary flexibility.[11−13] However, their large surface-to-volume ratio also results in an inherent instability with respect to the rapid grain growth even at moderate temperatures,[14] which leads to not only the vanishing of any favorable size-dependent properties but also the loss of structural integrity (easy breaking of the fibers). Commercial microscale alumina fibers (e.g., 3M Nextel 610 with diameters of 10−12 μm) can bear temperatures as high as 1100 °C against grain growth. However, the application of nanocrystalline oxide nanofibers at high temperatures such as flue-gas filtration, refractories, catalyst supports, and structural (reinforcing) or functional components in ceramic matrix composite is hampered as severe grain growth can occur at substantially lower temperatures when the fiber diameter is reduced to nanoscale, being stable only below ∼300−400 °C.[15]

Thus, the temperature-stability of nanocrystalline nanofibers not only represents a scientifically interesting (yet unsolved) problem but also remains as a major technological challenge hindering their widespread applications, despite the extensive studies for several decades.

Numerous efforts have been devoted to suppressing the grain growth thermodynamically via reducing grain boundary energy as the driving force or kinetically via Zener (secondary phase) pinning and solute drag effect for bulk nanocrystalline materials that have macroscopic dimensions and <100 nm grain sizes.[16−25] A rapid grain growth would occur at much lower temperatures in the nanofibers than that in the bulk materials but its underlying mechanism is still unclear. Herein, we used hot-stage in situ scanning transmission electron microscopy (STEM) to show that the enhanced grain growth in the oxide nanofibers is initiated at surfaces. Subsequently, we developed a new strategy to use an amorphous alumina surface nanocoating

(of ∼5 nm thick) to effectively inhibit the grain growth in nanofibers (∼200 nm in diameter) of our primary model material, 10 mol % scandia-stabilized zirconia (10ScSZ), as well as samarium-doped ceria (SDC), yttrium-stabilized zirconia (YSZ) and lanthanum molybdate ($La_2Mo_2O_9$). Such inhibition of grain growth improved the thermal stability of nanofibers with their operating temperature being increased by 400 °C, reaching 1100 °C; it also endowed the fibers with outstanding mechanical flexibility and other properties, such as suppressing the detrimental phase transformation that led to 10 times increase in the ionic conductivity.

Alumina, a stable, high-temperature oxide that does not react with, and has low solubility in, the oxides (10ScSZ, YSZ, ZrO_2, $La_2Mo_2O_9$, and SDC) used for making nanofibers in this study, was selected as the nanocoating material. The nanoscale coatings were applied by using the coaxial electrospinning method, which is facile, cost-effective, and scalable to fabricate nanofibers. As shown in Figure S1A, an Al-containing outer solution and a Sc- and Zr-containing inner solution were separately injected into a coaxial syringe. The viscosity and diffusion rate of the precursor solutions were carefully controlled. We inspected the morphology of the annealed coated nanofiber by scanning electron microscopy (SEM). The nanofibers were uniform throughout the entire length, exhibiting a cylindrical shape that is similar to that of the neat uncoated nanofibers (Figure S1B). An amorphous shell of 5 nm thick was evident in the high-resolution transmission electron microscopy (HRTEM) images (Figure 1A). Furthermore, the nanofibers were embedded in epoxy, sliced by
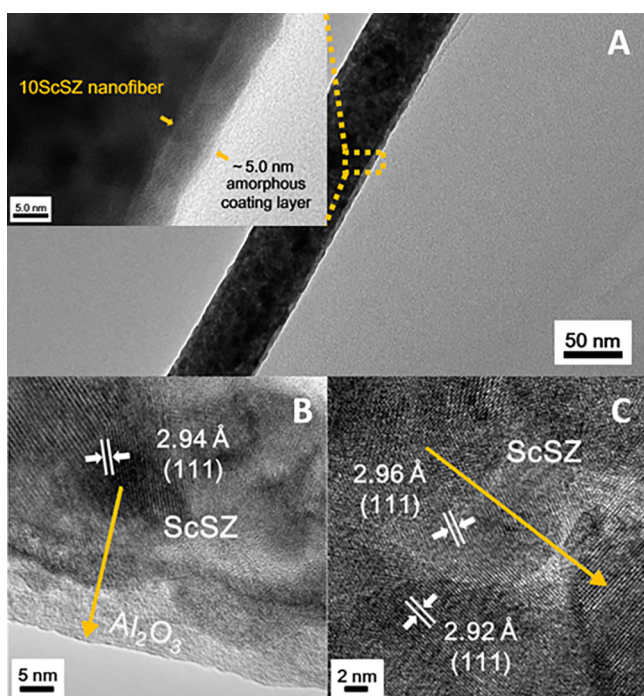
Figure 1. TEM images of the coated 10ScSZ nanofibers. (A) A typical TEM image of amorphous alumina-coated 10ScSZ nanofibers. The inset shows a high-magnification TEM image of surface of the nanofiber for the selected region marked by the orange rectangle with dashed line. HRTEM images of (B) surface and (C) inner region of the alumina coated 10ScSZ nanofibers. The orange arrows indicate the areas for the line-scan EDS analysis for Al element and the EDS results are shown in Figure S2.

microtome, and examined by HRTEM. We analyzed the composition distribution of the coated nanofibers by line-scan energy-dispersive X-ray spectroscopy (EDS) performed in STEM mode. Al atoms were detected in the amorphous nanocoating layers (Figure 1B and Figure S2A). X-ray photoelectron spectroscopy (XPS) analysis of Al 2p peak at ∼74.4 eV and the O 1s peak at ∼530 eV indicated the formation of Al—O bonds (Figure S3). The well-crystallized 10ScSZ grains in the core region of nanofibers showed the fringes associated with a cubic structure (Figure 1C), whereas EDS revealed few Al atoms inside the nanofiber (Figure S2B). Thus, the combination of HRTEM, STEM, EDS, and XPS results unequivocally confirmed the presence of ∼5 nm-thick amorphous alumina nanocoatings on the surface of 10ScSZ nanofibers (with ∼200 nm diameters and <10 nm crystallite sizes).

We believe that it is essential to make the nanoscale coating amorphous 1) to avoid a high crystal—crystal interface energy with the underneath fiber that may destabilize the nanocoating and 2) to ensure smooth surfaces and uniform coatings. Such an amorphous nanocoating strategy should be applicable to other nanodimensional, nanocrystalline materials with a large surface-to-volume ratio to suppress the surface-initiated grain growth (but not bulk nanocrystalline materials).

The morphologies of the alumina coated and uncoated 10ScSZ nanofibers annealed at different temperatures are shown in Figure 2A−D and Figure 2E−H, respectively. The grain sizes of the coated nanofibers were much smaller than those of the uncoated ones. The uncoated nanofibers annealed at 700 °C exhibited smooth surfaces (Figure 2E); however, significant grain growth was observed at a higher temperature. Consequently, the surfaces of the uncoated nanofibers were significantly roughened after annealing at 900 °C (Figure 2F). A so-called bamboo-like morphology appeared when the temperature was greater than 1000 °C (Figure 2G,H), whereby nanofibers became fragile and were easy to break from the necks, or the intersections (classical Mullins grooves in the nanofiber geometry) of the grain boundary and fiber surface. By contrast, the grain growth was significantly suppressed in alumina-coated nanofibers with smooth surface after annealing at 1100 °C (Figure 2D). Moreover, surfaces of coated nanofibers remained smooth even after annealing for 80 h at 1000 °C, whereas the uncoated nanofibers broke into segments because of substantial grain growth (Figure 2I and Figure S4).

We calculated the average crystallite size of the alumina-coated and -uncoated 10ScSZ nanofibers using the Scherer equation from X-ray diffraction (XRD) peaks and further verified these XRD crystallite sizes by direct TEM observation. For TEM measurements, we used ImageJ to quantify the grain size. The crystallite size versus annealing temperature curve was plotted in Figure 3A, which shows that grain growth was effectively suppressed in the coated nanofibers even at temperatures as high as 1100 °C. Interestingly, the reduced grain size of alumina-coated nanofibers stabilized the high-temperature cubic phase to room temperature (presumably due to the effect of retaining nanocrystallinity, where the high-temperature, high-symmetry phase is stabilized because of its smaller interfacial energy, akin to those reported for ZrO_2 and other oxide nanoparticles[26,27]), whereas a cubic-to-β phase transition occurred in the uncoated nanofibers (Figure S5). Notably, 10ScSZ nanofibers coated with amorphous alumina layers could withstand a long-term heating at 850 °C even after 80 h, showing a stable crystallite size of ∼7 nm that is
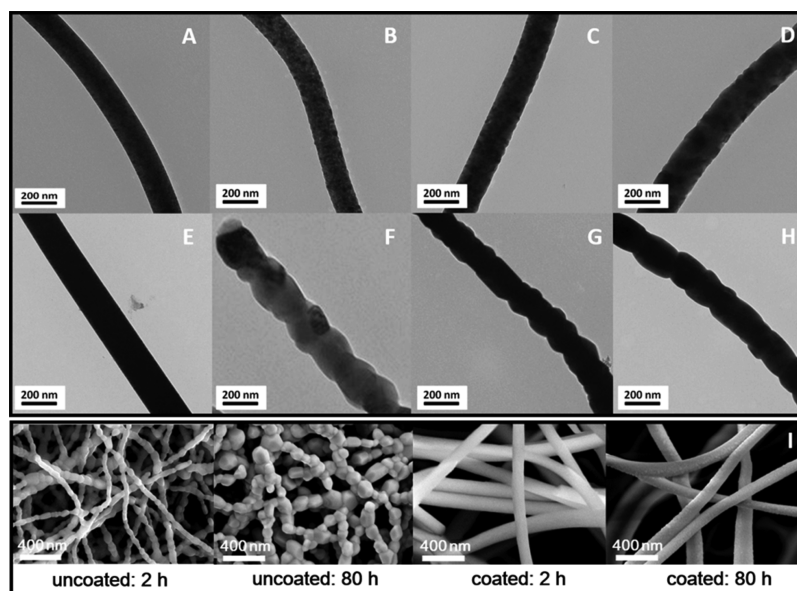
Figure 2. Grain growth of uncoated and coated 10ScSZ nanofibers. TEM images of amorphous alumina coated 10ScSZ nanofibers annealed at (A) 700 °C, (B) 900 °C, (C) 1000 °C, and (D) 1100 °C and uncoated 10ScSZ nanofibers annealed at (E) 700 °C, (F) 900 °C, (G) 1000 °C, and (H) 1100 °C. (I) SEM images for uncoated 10ScSZ nanofibers and alumina coated 10ScSZ nanofibers annealed at 1000 °C for 2 and 80 h, respectively.
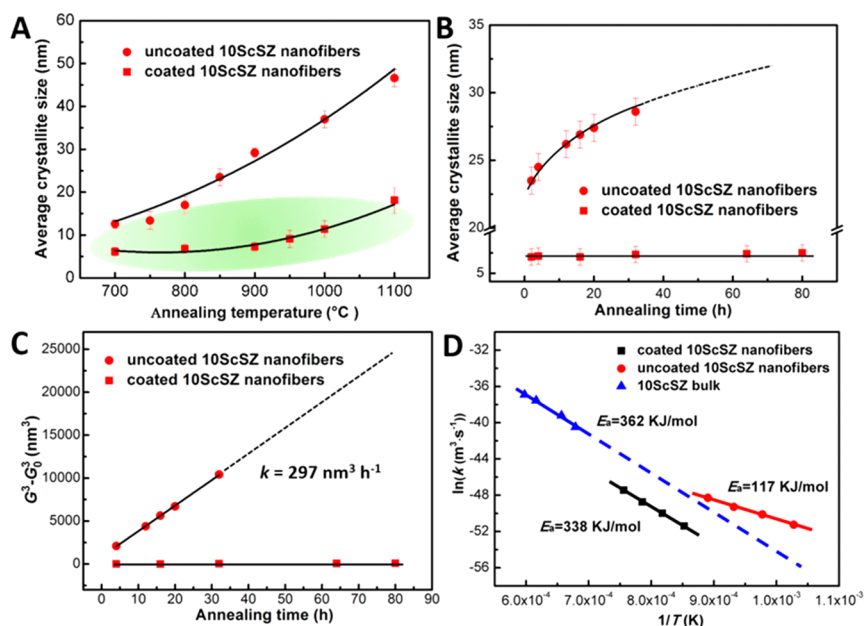
Figure 3. Grain growth kinetics. (A) Average crystallite sizes of the amorphous alumina coated 10ScSZ nanofibers and uncoated nanofibers at different annealing temperatures. (B) The average crystallite size of alumina coated and uncoated 10ScSZ nanofibers annealed at 850 °C for different durations. (C) The grain growth rate k for uncoated 10ScSZ nanofibers and alumina coated 10ScSZ nanofibers annealed at 850 °C. (D) The Arrhenius plots for calculating the grain-growth activation energy applied to data for 10ScSZ nanofibers with and without alumina coating layer.

essentially unchanged along with a stable cubic phase (Figure 3B). By contrast, the crystallite size of the uncoated 10ScSZ nanofibers increased with the annealing time and the cubic-to-β phase transition began to occur after 32 h.

The effect of nanocoatings on grain growth in the nanofibers was determined quantitatively (Figure S6). As a benchmark, the grain growth in a 10ScSZ bulk material was also investigated (Figure S7), where the grain sizes were determined from the cross-sectional SEM images (Figure S8). A classic equation describing the relationship between the grain size G and the annealing time t, $G_n - G_{0n} = k (t - t_0)$,[28] was used, where t_0 is 2 h, G_0 is the crystallite size at t_0, and n is an exponent related to

growth mechanism and is usually in the range from 1 to 4. Setting n at 3, a good linear relationship was found between ($G^3 - G_0^3$) and ($t - t_0$) (Figure 3C; Figures S6 and S9), and the growth rate constant k can be obtained from fitting. Specifically, we estimated the k values for the coated and uncoated nanofibers as well as the bulk 10ScSZ material at different temperatures. By plotting the logarithm of k against the reciprocal of absolute temperature, the apparent activation energy E of grain growth can be derived from the slope of the linear fittings (Figure 3D). The activation energy of the uncoated nanofibers (117 kJ/mol) is approximately one-third of that of bulk material (362 kJ/mol), whereas the value for the
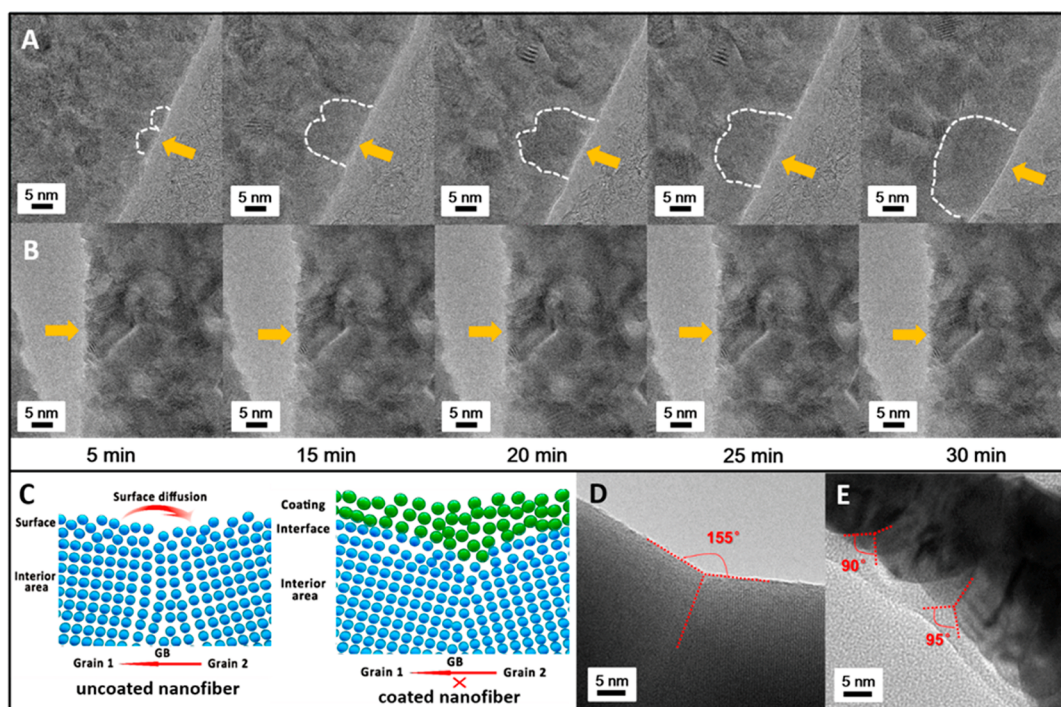
Figure 4. In situ and ex situ TEM images of nanofibers. A series of in situ TEM images of locations close to surface (marked by orange arrows) that recorded (A) grain growth in a 10ScSZ nanofiber and (B) no observable grain growth in an alumina-coated 10ScSZ nanofiber, both of which were annealed at 850 °C for 2 h. The images were taken at the times of 5, 15, 20, 25, and 30 min. The lattice fringes cannot be clearly discerned in this set of in situ STEM images at the current magnification; a higher-magnification HRTEM image for the inspected nanofiber in B is shown in Figure S10, where the lattice fringes and the surface amorphous coating can be clearly resolved. (C) Schematic illustration of the surface-initiated grain coarsening in an uncoated nanofiber and its inhibition by the nanocoating layer. The red cross means the movement of the grain boundary is significantly suppressed. TEM images of the surface of the (D) uncoated and (E) coated 10ScSZ nanofibers. The red dashed lines show the dihedral angles of grains at the surface of 10ScSZ nanofibers.

coated nanofiber (338 kJ/mol) is very close to the value for the bulk. This suggests that grain growth in the uncoated nanofibers is substantially easier than that in the bulk counterpart. Moreover, the significantly reduced activation energy of the uncoated fibers indicates a different mechanism that should be related to their high surface-to-volume ratios. The alumina nanocoatings are effective to suppress the grain growth so that the coated nanofibers exhibit an activation energy for grain growth that is similar to that of the bulk material.

To reveal the underlying mechanism of the enhanced grain growth in the uncoated nanofibers as well as the suppressing effect of the nanocoatings, in situ TEM observations were conducted at 850 °C.[29] Figure 4A,B shows the TEM images for the uncoated and coated 10ScSZ nanofibers, respectively, collected at an interval of 5 min. An HRTEM image of the coated 10ScSZ nanofiber is shown in Figure S10. First, we observed that the enhanced grain growth in the uncoated 10ScSZ nanofibers is initiated at the fiber surfaces (Figure 4A and see Supplementary Movie 1). As indicated by the orange arrows, nanograins at the surface of the fiber grew with grain boundaries moving perpendicular to the fiber surface (Figure S11), whereas growth of grains inside the fiber was negligible. We hypothesize that such surface-initiated grain growth of the uncoated nanofibers are facilitated by the lower activation energy of surface diffusion (that should be lower than activation energy both for grain boundaries and bulk diffusion) (Figure 4C), which is consistent with the observed lower activation energy for grain growth in the uncoated nanofibers. Noting that surface diffusion alone cannot result in grain boundary

migration and grain growth, so that the surface-initiated grain growth must be assisted by (most likely) grain boundary diffusion. Perhaps more importantly (than the surface-diffusion assisted grain growth), the anisotropic surface energy (for grains with different surface orientations) may also provide additional thermodynamic driving forces for the surface-initiated grain growth, wherein nanograins with a lower-energy surface have a higher thermodynamic tendency to grow.

Unlike the uncoated nanofibers, grain growth was not observed in the amorphous alumina coated nanofibers, neither at the surface nor in the inner part, during in situ TEM observation at 850 °C for 2 h (Figure 4B and see Supplementary Movie 2), thereby implying that the nanocoating inhibited the surface-initiated rapid grain growth observed in uncoated nanofibers. While similar surface-initiated grain growth mechanisms in thin films are known (or at least been widely speculated),[30,31] this work directly observes the surface-initiated rapid grain growth in (uncoated) oxide nanofiber and demonstrates its suppression by nanocoatings, for the first time to our knowledge.

To further understand the underlying mechanism of the alumina nanocoating on suppressing the surface-initiated rapid grain growth in the nanofibers, we analyzed the relative interfacial energies of the uncoated and coated nanofibers by examining the dihedral angle at surface grooves. HRTEM images of uncoated and coated 10ScSZ nanofiber slices from 20 nanofibers were inspected where dihedral angles were measured (Figure S12). The dihedral angle (ϕ) at a thermodynamic equilibrium was determined by a balance of the surface and grain boundary energies:[32,33] $2\gamma_{surface} \sin(\phi/2) = \gamma_{gb}$, where
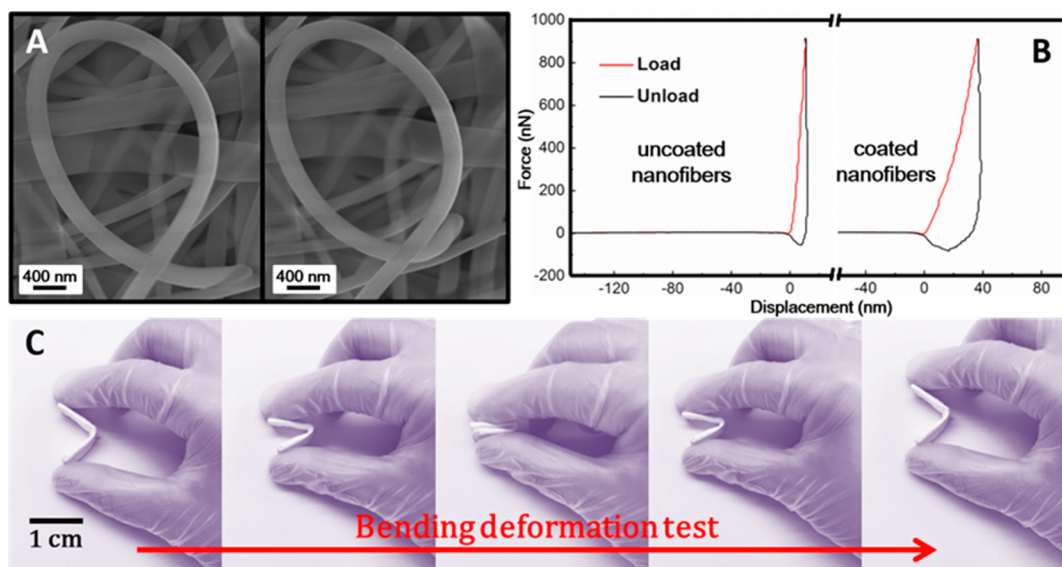
Figure 5. Bending properties of the coated nanofibers. (A) SEM images of amorphous alumina coated 10ScSZ nanofibers, which indicates the self-bending behavior of the fiber under the electron irradiation. (B) Force-deformation curves of uncoated and amorphous alumina coated 10ScSZ nanofiber annealed at 1000 °C. (C) Photographs for a coated nanofiber mat bent to different angles.

$\gamma_{surface}$ and γ_{gb} are surface energies (noting that $\gamma_{surface}$ includes effect of nanocoatings for the case of coated nanofibers) and grain boundary energies, respectively. The average dihedral angle decreased from $(150 \pm 4)°$ in the uncoated nanofibers to $(92 \pm 4)°$ in the amorphous alumina-coated nanofibers (Figure 4D,E).

On the basis of the above observations from in situ TEM and measurements of dihedral angles as well as other considerations, we propose following three possible (two kinetic and one thermodynamic) mechanisms for amorphous alumina nanocoatings to suppress surface-initiated rapid grain growth in nanocrystalline oxide nanofibers. First, atomic diffusions along the amorphous alumina-10ScSZ interface should be slower than that on the free surface, which would suppress the surface-diffusion assisted rapid growth of surface grains kinetically. Second, a smaller dihedral angle at the surface groove provides a greater pinning effect for surface grains to grow (i.e., "drag" the grain boundary migration perpendicularly to the fiber surface), providing a mechanism of nanocoatings to suppress the surface-initiated grain growth kinetically. Third, a smaller dihedral angle also suggests a lower surface energy (i.e., the interfacial energies with amorphous alumina are smaller than those for the free surface on average). As the anisotropy in surface energy can serve as a thermodynamic driving force for the surface-initiated grain growth, a lower mean surface energy can suppress the growth of certain surface grains thermodynamically.

To exclude the effect of possible dissolution and grain boundary segregation of Al in 10ScSZ phase on hindering grain growth either thermodynamically or kinetically, we incorporated Al_2O_3 into 10ScSZ nanofibers with different alumina contents for comparison. The results show that the addition of Al_2O_3 directly into the matrix of 10ScSZ nanofibers did not suppress the grain growth as significant as that in the cases of surface-coated fibers. The Al_2O_3-containing fibers exhibited a bamboo-like morphology after annealing at 1000 °C, and β phase cannot be avoided in the fibers when cooled to room temperature (Figures S13 and S14). These comparisons further

support the previously proposed surface-initiated grain growth mechanism and its suppression mechanisms by nanocoatings.

The method of suppressing the grain growth can also be extended to other nanocrystalline oxide nanofibers. Amorphous alumina nanocoatings can also stabilize nanocrystalline ZrO_2, YSZ, SDC, and $La_2Mo_2O_9$ nanofibers against grain growth at high temperatures, as evident from Figure S15, and no secondary phase was detected in any case (Figure S16). Therefore, both newly observed surface-initiated grain growth mechanism and the proposed innovative suppression method by nanocoating are likely applicable to various oxide nanofibers. These findings pave the way for applications of high-performance nanofibers at moderate and high temperatures for a broad range of applications.

Yet another challenge is that the flexibility of nanocrystalline oxide nanofibers is difficult to maintain after exposures to high temperatures (unavoidable during the fabrication or service). For example, 10ScSZ nanofibers annealed at 550 °C are flexible. However, after annealing at 1000 °C, the uncoated nanofibers became fragile due to severe grain growth and the formation of bamboo-like structure (Figure 2G). It is difficult to pick up such fibers without damaging them. In a striking contrast, the amorphous alumina-coated 10ScSZ nanofibers still showed excellent flexibility after annealing at 1000 °C (Figure 5A and Figure S17). The fibers can be bent and even knitted into a circle under electron irradiation during the SEM inspections, resembling the behavior of flexible polymer fibers.[34−36] Moreover, force−displacement ($F−d$) curves of uncoated and coated 10ScSZ nanofibers were acquired from the nanomechanical tests using atomic force microscopy (AFM) (Figure S18 and Figure 5B).[37] The more significant deviation of the unloading curve from the loading curve for the coated 10ScSZ nanofibers than the uncoated ones also suggested a higher flexibility for the former fibers. Given the exceptionally high flexibility of the coated oxide nanofibers, the as-prepared nanofiber mat (prepared by electrospinning for 6 h and a subsequent calcination at 1000 °C for 2 h) can be deformed with a bending angle of 180° without obvious fractures (Figure 5C). As the pressing force was released, it can

be recovered by itself to a bending angle of 100° within 1−2 s. A bending test for the coated nanofiber mat was conducted with a bending radius of 5 mm for 1000 cycles (Supplementary Movie 3). It can be seen clearly that the fiber mat did not fracture and can still hang a clip after the bending test.

The electrical (ionic) properties of the coated 10ScSZ nanofibers were also examined (the testing configuration is shown in Figure S19 and typical impedance spectra are shown in Figure S20A). Figure S20B shows the temperature dependency of the ionic conductivity of coated and uncoated 10ScSZ nanofibers annealed at the same temperature and that of bulk 10ScSZ material. Conductivity drops were observed in the curves of the uncoated nanofibers and the bulk material, which is associated with the detrimental phase transition from the highly conductive cubic phase to the less conductive β phase.[38] In contrast, such drops were not observed in the coated nanofibers because of inhibition of cubic-to-β phase transition by nanocoatings which leads to an increase in conductivity by 1 order of magnitude. For the coated nanofibers, the conductivities measured at 550 and 600 °C remained almost constant with the decrease of oxygen partial pressure (Figure S21), indicating that the nanofibers are pure ionic conductors and electronic conduction is negligible. As demonstrated above, such a strategy of using amorphous alumina nanocoatings to stabilize the highly conductive phase can also be applied to other ionic conductors such as YSZ and $La_2Mo_2O_9$ that also suffer from the transitions from a high-temperature, high-symmetry, and high-conductive phase to a low-temperature, low-symmetry, and low-conductive phase, which can be stabilized by maintaining the small grain size.[11] Therefore, these results demonstrate a new strategy to tailor the crystal structure (temperature-dependent phase stability) and electrical properties of oxide nanofibers for the next-generation solid-state electrochemical devices.

In summary, this study uncovered the mechanism of surface-initiated rapid grain growth in the nanocrystalline oxide nanofiber that has a significantly lower grain growth activation energy than that of the bulk counterparts. We further developed a facile yet innovative method to use nanoscale amorphous alumina coating to suppress the surface-initiated rapid grain growth of the nanofibers. The nanocoating can suppress the detrimental phase transformation to stabilize a high-temperature, high-conductive, cubic phase in 10ScSZ and other similar oxide nanofibers, thereby resulting in a 10-fold increase in the ionic conductivity. The coated oxide nanofibers showed exceptional high-temperature stability and flexibility even after annealing at the high temperatures. As numerous promising properties of oxide nanofibers rely on their nanoscale dimensions and nanocrystallinity, the mechanistic understanding and innovative nanocoating strategy developed in this work would pave the way for widespread applications of these important nanomaterials.

ASSOCIATED CONTENT

Ⓢ Supporting Information

The Supporting Information is available free of charge on the ACS Publications website at DOI: 10.1021/acs.nanolett.7b03651.

Methods and additional experimental data (PDF)

In situ TEM results (AVI)

In situ TEM results (AVI)

In situ TEM results (AVI)

AUTHOR INFORMATION

Corresponding Authors

*E-mail: panw@mail.tsinghua.edu.cn (W.P.).
*E-mail: jluo@alum.mit.edu (J.L.).

ORCID Ⓘ

Lei Yao: 0000-0001-5289-7970
Jian Luo: 0000-0002-5424-0216

Author Contributions

L.Y. conceived the idea, performed the experiment, analyzed the data, and wrote the manuscript. W.P. guided and supervised the experiments and analysis. J.L. analyzed the data and contributed to writing and editing the manuscript. J.C., X.Z., and H.N. performed some experiments. All authors discussed the results and commented on the paper.

Notes

The authors declare no competing financial interest.

REFERENCES

(1) Lu, K.; Lu, L.; Suresh, S. *Science* **2009**, *324*, 349−352.
(2) Hu, J.; Shi, Y. N.; Sauvage, X.; Sha, G.; Lu, K. *Science* **2017**, *355*, 1292−1296.
(3) Feng, B.; Yokoi, T.; Kumamoto, A.; Yoshiya, M.; Ikuhara, Y.; Shibata, N. *Nat. Commun.* **2016**, *7*, 11079.
(4) Bae, K.; Jang, D. Y.; Choi, H. J.; Kim, D.; Hong, J.; Kim, B.-K.; Lee, J.-H.; Son, J.-W.; Shim, J. H. *Nat. Commun.* **2017**, *8*, 14553.
(5) Si, Y.; Yu, J.; Tang, X.; Ge, J.; Ding, B. *Nat. Commun.* **2014**, *5*, 5802.
(6) Torres Galvis, H. M.; Bitter, J. H.; Khare, C. B.; Ruitenbeek, M.; Dugulan, A. I.; de Jong, K. P. *Science* **2012**, *335*, 835−838.
(7) Poudel, B.; Hao, Q.; Ma, Y.; Lan, Y.; Minnich, A.; Yu, B.; Yan, X.; Wang, D.; Muto, A.; Vashaee, D.; Chen, X.; Liu, J.; Dresselhaus, M. S.; Chen, G.; Ren, Z. *Science* **2008**, *320*, 634−638.
(8) Lu, L.; Shen, Y.; Chen, X.; Qian, L.; Lu, K. *Science* **2004**, *304*, 422−426.
(9) Wang, Y.; Chen, M.; Zhou, F.; Ma, E. *Nature* **2002**, *419*, 912−915.
(10) Ishikawa, T.; Yamaoka, H.; Harada, Y.; Fujii, T.; Nagasawa, T. *Nature* **2002**, *416*, 64−67.
(11) Liu, W.; Pan, W.; Luo, J.; Godfrey, A.; Ou, G.; Wu, H.; Zhang, W. *Nat. Commun.* **2015**, *6*, 8354.
(12) Eckel, Z. C.; Zhou, C.; Martin, J. H.; Jacobsen, A. J.; Carter, W. B.; Schaedler, T. A. *Science* **2016**, *351*, 58−62.
(13) Wang, H.; Zhang, X.; Wang, N.; Li, Y.; Feng, X.; Huang, Y.; Zhao, C.; Liu, Z.; Fang, M.; Ou, G.; Gao, H.; Li, X.; Wu, H. *Sci. Adv.* **2017**, *3*, e1603170.
(14) Ames, M.; Markmann, J.; Karos, R.; Michels, A.; Tschope, A.; Birringer, R. *Acta Mater.* **2008**, *56*, 4255−4266.
(15) Ma, Y.; Wang, X.; Li, S.; Toprak, M. S.; Zhu, B.; Muhammed, M. *Adv. Mater.* **2010**, *22*, 1640−1644.
(16) Luo, J.; Cheng, H.; Asl, K. M.; Kiely, C. J.; Harmer, M. P. *Science* **2011**, *333*, 1730−1733.
(17) Baram, M.; Chatain, D.; Kaplan, W. D. *Science* **2011**, *332*, 206−209.
(18) Kahlweit, M. *Science* **1988**, *240*, 617−621.
(19) Millett, P. C.; Selvam, R. P.; Saxena, A. *Acta Mater.* **2007**, *55*, 2329−2336.

(20) Detor, A. J.; Schuh, C. A. *Acta Mater.* **2007**, *55*, 4221−4232.

(21) Choi, P.; da Silva, M.; Klement, U.; Al-Kassab, T.; Kirchheim, R. *Acta Mater.* **2005**, *53*, 4473−4481.

(22) Mayr, S. G.; Bedorf, D. *Phys. Rev. B: Condens. Matter Mater. Phys.* **2007**, *76*, 024111.

(23) Chookajorn, T.; Murdoch, H. A.; Schuh, C. A. *Science* **2012**, *337*, 951−954.

(24) Chen, I.-W.; Wang, X.-H. *Nature* **2000**, *404*, 168−171.

(25) Kirsch, B. L.; Riley, A. E.; Gross, A. F.; Tolbert, S. H. *Langmuir* **2004**, *20*, 11247−11254.

(26) Castro, R. H. R. *Mater. Lett.* **2013**, *96*, 45−56.

(27) Navrotsky, A.; Ma, C.; Lilova, K.; Birkner, N. *Science* **2010**, *330*, 199−201.

(28) Quach, D. V.; Avila-Paredes, H.; Kim, S.; Martin, M.; Munir, Z. A. *Acta Mater.* **2010**, *58*, 5022−5030.

(29) Hudak, B. M.; Depner, S. W.; Waetzig, G. R.; Talapatra, A.; Arroyave, R.; Banerjee, S.; Guiton, B. S. *Nat. Commun.* **2017**, *8*, 15316.

(30) Erk, K. A.; Deschaseaux, C.; Trice, R. W. *J. Am. Ceram. Soc.* **2006**, *89*, 1673−1678.

(31) Baek, I.-H.; Pyeon, J. J.; Song, Y. G.; Chung, T.-M.; Kim, H.-R.; Baek, S.-H.; Kim, J.-S.; Kang, C.-Y.; Choi, J.-W.; Hwang, C. S.; Han, J. H.; Kim, S. K. *Chem. Mater.* **2017**, *29*, 8100−8110.

(32) Mullins, W. W. *J. Appl. Phys.* **1957**, *28*, 333−339.

(33) Kaplan, W. D. *Science* **2015**, *349*, 1059−1060.

(34) Khalid, B.; Bai, X.; Wei, H.; Huang, Y.; Wu, H.; Cui, Y. *Nano Lett.* **2017**, *17*, 1140−1148.

(35) Yang, A.; Cai, L.; Zhang, R.; Wang, J.; Hsu, P.; Wang, H.; Zhou, G.; Xu, J.; Cui, Y. *Nano Lett.* **2017**, *17*, 3506−3510.

(36) Hao, X.; Zhu, J.; Jiang, X.; Wu, H.; Qiao, J.; Sun, W.; Wang, Z.; Sun, K. *Nano Lett.* **2016**, *16*, 2981−2987.

(37) Wang, W.; Barber, A. H. *J. Polym. Sci., Part B: Polym. Phys.* **2012**, *50*, 546−551.

(38) Yao, L.; Liu, W.; Ou, G.; Nishijima, H.; Pan, W. *J. Mater. Chem. A* **2015**, *3*, 10795−10800.